Self-consistent quasi-particle GW and hybrid functional calculations for Al/InAs/Al heterojunctions: band offset and spin-orbit coupling effects

H. Ness,[1] F. Corsetti,[2] D. Pashov,[1] B. Verstichel,[3] G. W. Winkler,[4] M. van Schilfgaarde,[1,5] and R. M. Lutchyn[4]

[1]*Department of Physics, Faculty of Natural and Mathematical Sciences, King's College London, Strand, London WC2R 2LS, UK*
[2]*Microsoft Azure Quantum, 2800 Lyngby, Denmark*
[3]*Synopsys Denmark, 2100 Copenhagen, Denmark*
[4]*Microsoft Azure Quantum, Goleta, California 93111, USA*
[5]*National Renewable Energy Laboratory, Golden, Colorado 80401, USA*

arXiv:2403.17809v4 [cond-mat.mes-hall] 20 May 2024

The electronic structure of surfaces and interfaces plays a key role in the properties of quantum devices. Here, we study the electronic structure of realistic Al/InAs/Al heterojunctions using a combination of density functional theory (DFT) with hybrid functionals and state-of-the-art quasi-particle GW (QSGW) calculations. We find a good agreement between QSGW calculations and hybrid functional calculations which themselves compare favourably well with ARPES experiments. Our study confirm the need of well controlled quality of the interfaces to obtain the needed properties of InAs/Al heterojunctions. A detailed analysis of the effects of spin-orbit coupling on the spin-splitting of the electronic states show a linear scaling in k-space, related to the two-dimensional nature of some interface states. The good agreement by QSGW and hybrid functional calculations open the door towards trust-able use of an effective approximation to QSGW for studying very large heterojunctions.

Keywords: electronic structure of surfaces and interfaces, density functional theory, hybrid functionals and many-body perturbation theory, quantum materials, III-V semiconductors

I. INTRODUCTION

Because of their unique combination of material parameters (i.e. large spin-orbit coupling, small effective mass, large Lande g-factor), narrow-gap III-V semiconductors (such as InAs or InSb) have generated considerable interest in many technological applications.

Recently, these materials have been central to the experimental realisation of the so-called Majorana zero modes[1–10]. In this devices, the main goal is to develop topological p-wave superconductivity at the interface of a conventional semiconductor and an s-wave superconductor. An exceptionally good control of the interface properties is needed to realise topological superconducting phases and to manipulate Majorana zero modes which are the key ingredient in topological quantum computation proposals[8,10–12]. The hybrid semiconductor-superconductor Majorana devices are required to have a large g-factor, strong Rashba spin-orbit coupling and significant proximity-induced superconducting gap. Recently, the proximity-induced superconductivity has been studied in devices made of a semiconductor nanowire in contact with a superconductor, including Al/InAs[13–19], Al/InSb[20–23] Pb/InAs[24], and Sn/InSb[25]. High-quality superconductor/semiconductor interfaces (i.e. uniform and transparent) are required to optimise the topological gaps in these heterostructures.

The geometry of the interface may give rise to (desirable or undesirable) interface states, it may alter the band bending and band alignment, or affect the magnitude of the proximity-induced gap and of the spin-orbit coupling. Understanding the resulting surface/interface states and Fermi-level pinning is important for engineering appropriate interface Hamiltonian and realising topological superconductivity hosting Majoranas.

Band bending and surface states have been observed by angle-resolved photoemission spectroscopy (ARPES)[26–28] and scanning tunneling microscopy and spectroscopy (STM/STS)[29]. First principles simulations based on density functional theory (DFT) can help interpret experiments and resolve the effects of the interfaces. DFT studies of InAs and InSb surfaces and interfaces have been limited because local (local density approximation LDA) and semi-local exchange-correlation functionals severely underestimate the band gap to the limiting point where it reduces to zero[30]. More accurate methods involving quasi-particle self-consistent GW (QSGW) approaches or hybrid functionals provide results much closer to the experimental (bulk) gap (0.42 eV for bulk InAs).

In this paper, we present calculations of realistic Al(111)/InAs(001) heterojunctions using a QSGW method implemented in the Questaal package. The QSGW results are also compared with hybrid functionals DFT calculations. We focus our attention on the effects of "disorder" (using numerical "experiments") on the electronic structure of realistic InAs/Al interfaces described at the atomic scale. The disorder we consider is coming from: (i) atomic relaxations (i.e. the atoms at the InAs/Al interfaces do not rest at their correspond bulk atomic positions), (ii) substitution disorder which mimics in a simple way potential atomic diffusion at the interface, and (iii) rescaling the spin-orbit coupling strength on some atoms which mimics the presence of some external electric fields at the interfaces.

The paper is organised as follows: In Section II, we present the InAs/Al system we considered and the two

software packages used for the electronic structure calculations, namely the Questaal and QuantumATK packages. The results of our calculations are shown and analysed in Section III, where we extract the profiles of the valence band maxima (VBM) and conduction band minim (CBm) along the InAs/Al heterojunction and study in details the effects of spin-orbit coupling (SOC) on some specific bands. Conclusions are presented in Section IV. Additional informations are provided in the appendices, about: the implementation of the Questaal code on GPUs in Appendix A, the hybrid functional in Appendix B, local density of states, and bulk versus heterojunctions bands in subsequent appendices.

II. CALCULATIONS

First principles electronic structure calculations have been performed using two different packages: the Questaal package[31] and the pseudopotential QuantumATK package[32].

Questaal is an all-electron method, with an augmented wave basis consisting of partial waves inside augmentation spheres based on the linear muffin-tin orbital (LMTO) technique[33]. It includes conventional DFT-based calculations, as well as many-body perturbation theory, especially with its implementation of a quasi-particle self-consistent GW (QSGW) approach[34,35].

We have considered InAs/Al heterojunctions for which the interface between the two materials is built from the (001) surface for InAs and from the (111) surface for Al, with As-terminated InAs surfaces in direct contact with the Al surface (as suggested by the experiments in[27]). We took a low temperature lattice parameter of $a_0 = 6.06$ Å for InAl, and a (001) surface supercell based on the two following (001) surface vectors $u_1 = [2, 0]a_0$ and $u_2 = [-1, 3]a_0$. For this (001) supercell, there are 6 atoms in each In (As) atomic planes perpendicular to the z-direction, see Fig. 1. For this supercell, one can match the Al(111) surface rather well, with a slight stretch (of 3%) in the u_2 direction, using a bulk lattice parameter of $a_{\rm Al} = 4.05$ Å. Then, each Al atomic plane parallel to the InAs/Al interface contains 15 atoms.

In order to minimise the computational cost, more specifically for the QSGW calculations, we have considered the minimal possible size for the junctions. We have found that to be able to keep the bulk-like character for the electronic structure in the middle of the InAs slab, one needs to go beyond a few layers of InAl: typically for 6 (7) atomic planes of In (As) (and beyond) we recover the bulk-like density of states for the In (As) atoms in the center of the InAs slab. As Al is a metal with a shorter screening length, fewer atomic layers are needed (typically 4 atomic (111) planes are enough) to obtain a bulk-like density of states in the central atomic layers.

Relaxation of the atomic positions have been performed within DFT-LDA. We have allowed the atoms in the Al atomic layers next to the interfaces, and the atoms of As and In in the two outmost atomic layers close to the InAs/Al interfaces to relax until the force components are below 10 mRy/bohr (257 meV/Å).

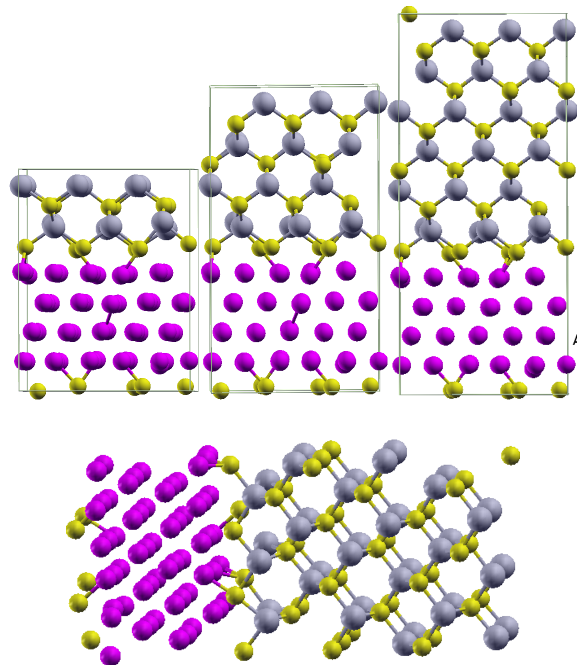

FIG. 1. (Top) Ball-and-stick representation of the relaxed InAs(001)/Al(111) supercell, for different number of InAs layers. In atoms are shown in grey, As atoms in yellow and Al atoms in purple. (Bottom) Side view of the InAs(001)/Al(111) atomic planes. The largest supercell contains 138 atoms with 4, 6, 7 atomic planes of In, As, Al respectively. Each plane contains either 6 atoms of In (As) or 15 atoms of Al.

We did not impose any symmetry during the atomic relaxation. Therefore the two InAs/Al interfaces of the supercell are not equivalent. This allows us to minimise the possible existence of unwanted electronic states that may have arisen due to size and coupling effects between two perfectly symmetric interfaces. To some extend, this can be also seen as a simplified case of "geometric" disorder.

In DFT-LDA and even in GW calculations, band gaps are often underestimated (LDA) or overestimated (GW). Indeed they should be because the RPA screened Coulomb interaction W is not sufficiently screened. Improvement of W by the addition of ladder diagrams indeed does improve the gaps[36,37]. In most of the cases, the dielectric constant of semiconductors and insulators is about 80% of the experimental value. This is because the ladder diagrams are missing in the RPA. However, these higher order diagrams are computationally costly, and here we adopt a simpler approach here. We have found that scaling the dielectric constant by 0.8, or alternatively using a hybrid of 80% QSGW and 20% LDA, we can mimic the effect of the ladders. This eliminates most of the errors.

Hence, we have use hybrid of LDA and QSGW functionals, $\Sigma^{\rm scaled} = \Sigma_{\rm QSGW} \times 0.8 + V_{\rm xc}^{\rm LDA} \times 0.2$, in the calculations of our band structures.

The system we considered contains 138 atoms (4×15 atoms of Al, 6×6 of In and 7×6 of As). To our knowledge, this is one of the first time that self-consistent QSGW calculations have been performed for such a "large" system. The Questaal package was re-developed and optimised to take advantage of GPU-based computing on a multi-petaflop modular supercomputer, see Appendix A.

We are interested in determining the profile of the valence band maxima (VBM) and of the conduction band minima (CBm) along the InAs/Al heterojunction. There are different ways to find such a profile, for example by considering the electrostatic potential of the heterojunction, or by considering the change in energy position of deep electronic levels of the junction in comparison to their bulk equivalent. Obviously, the profile of the VBM or CBm obtained from such atomic scale systems (for example, the thickness of the InAs slab in the 138 atom supercell is ~ 26.5 Å) will not reflect the band bending of Schottky barriers expected from a continuum model of the semiconductor/metal contact described on the micron scale. However our atomic scale calculations incorporate the more local effects of the InAs/Al interfaces against the bulk property of the materials.

To evaluate the profile of the valence (conduction) band maxima (minima), we extract the energy position of the deep electronic levels on each In atom (deep d-orbital) and each As atom (deep s-orbital). Assuming a rigid energy shift of these deep electronic levels relative to the Fermi level $E_{\rm F}$ in both the bulk and the heterojunction systems, we can determine the profile (averaged over the number of atoms in each atomic layer) of the VBM (along the main direction of the junction) relative to the exact QSGW Fermi level of the junction. The profile of the CBm is obtained from a rigid shift of the VBM by the bulk QSGW band gap (0.47 eV in the present case).

It is important to note that all the QSGW calculations were performed in the presence of spin-orbit coupling (SOC). Orbitals with s-like character are not affected by the presence of SOC. However the d-orbitals are split by the SOC. For bulk-like environment, the d-orbitals are split into two subsets according to the crystal symmetry. For In atoms close the Al/InAs interfaces the symmetry is reduced (further reduced by the atomic relaxations), and different energy shifts occur for the different d-orbitals on these atoms. There is more "fluctuation" of the energy shift for these atoms in comparison to bulk-like In atoms in the center of the InAs slab.

As a final comparison, we also perform calculations on the same system using a different methodology for correcting the band gap problem: hybrid functionals. Traditional hybrid functionals which use a fixed global mixing fraction α of Fock exchange can show limitations in the case of inhomogeneous interface systems, specifically if the different materials require different values of α to recover the correct bulk electronic structure and band gap. The situation is even more severe for the present case of semiconductor/metal interfaces.

To overcome this problem, we build on a recently developed scheme for a local (i.e., spatially-varying) mixing fraction, based on an estimator of the local dielectric constant defined as a functional of the electronic density[38,39]. In order to deal with the metallic region in our system, a second, metallic estimator, is introduced, which determines locally if the material is a metal, and, if so, sets α to zero. A more detailed explanation of the method can be found in Appendix B. We apply this scheme to the HSE06 functional[40]. We shall refer to these calculations as HSE06+DDH (dielectric-dependent hybrid).

The HSE06+DDH calculations are performed using the QuantumATK package[32] (version T-2022.03) within a pseudopotential and linear combination of atomic orbitals (LCAO) formalism. The calculations are carried out with a spin-polarized non-collinear Hamiltonian. We use norm-conserving pseudopotentials from the PseudoDojo[41] fully relativistic set and the medium basis set (LCAO-M[32]) from QuantumATK. The auxiliary density matrix method (ADMM)[42] is used to speed up the calculation of the exchange matrix.

The determination of the VBM/CBm is performed in the same way as for the QSGW calculations, i.e. by extracting the energy position of the core levels relative to $E_{\rm F}$. However, due to the configuration of the pseudopotentials, we use the semi-core d-orbitals for both In and As. The bulk InAs band gap obtained with HSE06+DDH is 0.47 eV, in agreement with QSGW.

III. RESULTS

A. Band alignment

Figure 2 shows the profile of the VBM in the InAl/Al heterojunctions. It corresponds to a shallow parabolic-like curve where the VBM is higher close to the InAs/Al interfaces than in the bulk-like part of InAs. Such a profile does not directly compare with conventional band-bending in Schottky barriers, the latter occurs on much larger length scales ($\sim \mu$m) than the scale corresponding to our atomic-scale calculations. However, the inflections of the VBM reflects the effect of the interfaces against the bulk, most certainly due to the presence of interface electric dipoles.

The dispersion in the energy shifts displayed by the symbols (red circles for the In deep d-orbital, green up-triangles for the As deep s-orbital) reflects that each atom in a given atomic layer are different. This is mostly true for the atoms near the InAs/Al interfaces which have been allowed to relax. Such a dispersion is minimal for the atoms in the center of the InAs slab where their position correspond to bulk unrelaxed atomic positions.

The QSGW calculations for bulk InAs provides a band gap 0.47 eV, close to the experimental band gap of 0.42 eV at low temperature. From that value, we can see

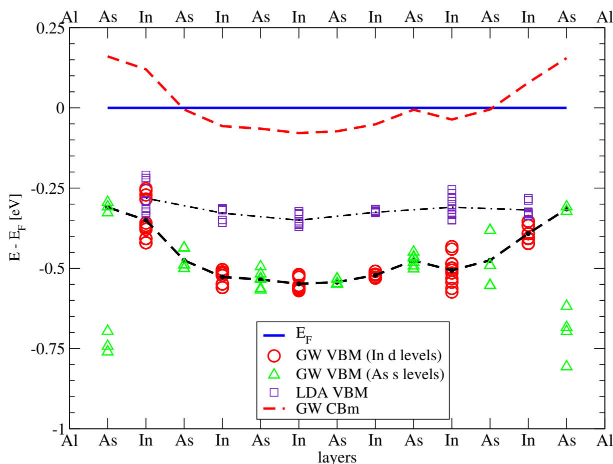

FIG. 2. Profile of the local valence band maximum (VBM) for the InAs/Al junction made of 138 atoms. Symbols represent the different shifted energy levels (deep In-d and As-s orbitals) of the In and As atoms located in each atomic plane along the main axis of the junction. Lines correspond to the averaged value of the energy shift in each atomic plane. The black dashed and dashed-dotted lines correspond to the QSGW and LDA VBM respectively. The red dashed line is the QSGW conduction band minima (CBm), i.e. the VBM shifted by the QSGW bulk band gap. Blue line presents the Fermi level $E_{\rm F}$ position. Both QSGW and LDA have been shifted to correspond to this energy reference $E_{\rm F} = 0$. The QSGW CBm lies ~80 meV below $E_{\rm F}$ in the center of the InAs slab.

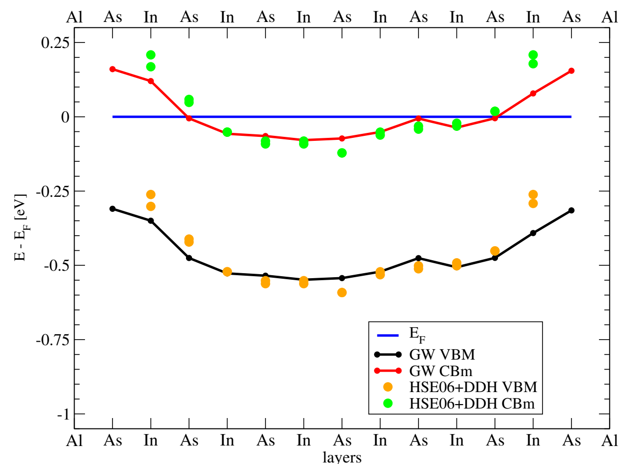

FIG. 3. Profile of the local VBM and CBm for the InAs/Al junction obtained from QSGW (same values as in Figure 2) and HSE06+DDH. The agreement between the two methods is particularly good.

that the CBm (obtained from rigid shift of the VBM) crosses the Fermi level of the junction. The CBm lies below $E_{\rm F}$, by an amount of ~80 meV, in the "bulk" part of the InAs slab.

This prediction of an accumulation layer in InAs is in agreement with ARPES measurements[27], although the band offset extracted from experiment is larger than what is seen in our simulation cell. For quantitative agreement, convergence to larger cells is probably needed.

For this, we turn to our hybrid functional calculations using the HSE06+DDH method. This method represents a more empirical and less accurate approach than QSGW, but also significantly less demanding of computational resources, and therefore potentially able to scale to larger systems. Figure 3 shows the comparison of the local band edges calculated with QSGW and HSE06+DDH. The overall shape of the band edges is well reproduced by HSE06+DDH, and there is an excellent quantitative agreement in the bulk of the semiconductor (within two layers of the interface). As an additional check, we have also compared the LDA band edges calculated with the package Questaal (shown in Figure 2) with QuantumATK (not shown) and recovered a similar good agreement. Therefore, the HSE06+DDH method provides an effective approximation to the full QSGW for this system, and might be used to explore much larger interface cells or multiple different interface configurations at a lower computational cost.

In order to get a better understanding of the effects of disorder at the InAs/Al interfaces on the energy level alignment, we have considered the following "numerical experiment".

We simulate the possible atomic diffusion at the interfaces by substituting some atoms by others. From the valence properties of In, As and Al, it appears reasonable to envisage substitutional disorder between In and Al atoms. We have therefore considered InAs/Al interfaces for which some In atoms (in the atomic layers closest to the interfaces) are replaced by Al atoms.

There are many possible combinations to realise such substitutions, and we have considered only a few of them. We started by replacing only one In atom by one Al atom in the In atomic layer located the closest to the the right InAs/Al interface, see labels for the atomic planes in Figure 4. We have performed calculations for only two cases over the six possible cases of one atom substitution. The results for the VBM profile for one of this case is shown in Figure 4. We have also considered one case in which two In atoms are swapped by two Al atoms and we have found similar trends for the profile of the VBM. Our calculations indicate that the VBM is pushed down, by a further ~100 meV, to lower energy in the case of the "dirty" interfaces compared to the case of "perfect" interfaces.

B. Spin-orbit coupling effects

The presence of Rashba-like spin-orbit coupling (SOC) in narrow-gap InAs semiconductors is one of the central ingredients for inducing superconducting property by proximity of an s-wave superconductor like Al. Once superconducting, a InAs nanowire can eventually hosts

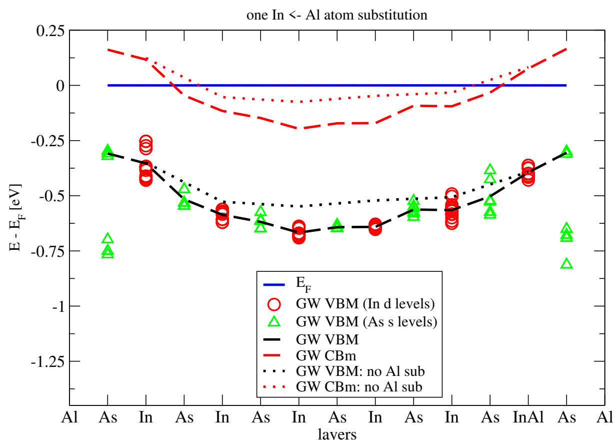

FIG. 4. Profile of the local valence band maximum (VBM) for the InAs/Al junction with similar notations as in Fig 2. Comparison between perfect and "disordered" interfaces. One atom of In is replaced by one Al atom in the In atomic plane closest to the right InAs/Al interface (see label InAl on the horizontal axis). All calculations are performed with QSGW. The VBM/CBm are pushed down to lower energy in the case of the "dirty" interface, i.e. compare dashed-lines with dotted-lines (black for VBM, red for CBm). "Interface disorder" seems to push the CBm down by a further $\sim$ 100 meV. A similar behaviour has also been obtained in two different cases of one In $\leftarrow$ Al atom substitution (the Al atom is located at a different site in the corresponding In atomic plane), as well as for a case of 2 In $\leftarrow$ Al atoms substitution in the corresponding In atomic plane.

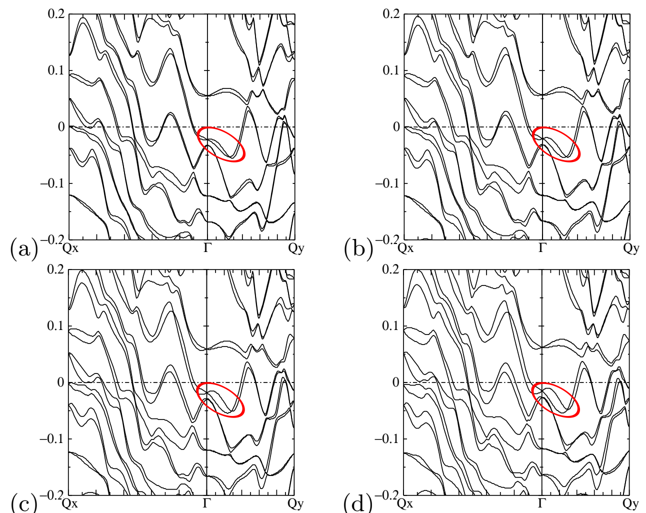

FIG. 5. QSGW band structure of the InAs/Al heterojunction made of 138 atoms, for different rescaling of the SOC. Panel (a), (b), (c) and (d) corresponds to rescaling the original SOC by $\times 2, \times 3, \times 4$ and $\times 5$ respectively. Focusing on the bands around the Γ point and at $E \sim E_{\rm F} - 0.05$, one can see the spin-split bands (due to SOC) along the $\Gamma - Qy$ direction. The splitting between the two bands increases with increasing rescaling of the SOC. The band encircled in red corresponds to the bottom of the bulk InAs conduction band in the case of the junction (see Appendix C 3).

a pair of Majorana state at each of its ends where the superconducting order parameter vanishes.

In the previous section, we have studied how band alignment in InAs deviates from pure bulk to InAs/Al interfaces, including some form of disorder of the interfaces.

We now consider the possibility of another type of disorder and its effects on the band structure of the InAs/Al junction. For that we now consider the following numerical "experiment": the strength of the SOC, on some atoms in the system, is rescaled to larger values. The SOC rescaling is applied on either all the In and As atoms or only on the In and As atoms close to the InAs/Al interfaces (i.e. In atoms labelled $z = 12, z = 27$ and As atoms labelled $z = 0.3, z = 10$ in panel (d) for Fig. 7). Note that a light element like Al does not have strong SOC and rescaling the SOC on Al is not relevant. The increase of the SOC can be seen as an indirect effect of the presence of an extra external electric field (perpendicular to the InAs/Al interface in the case of Rashba-like SOC) due to gating or other effects not taken into account in our model of the InAs/Al heterojunction.

In Appendix C 3, we show how the band structure of the InAs/Al junction differs strongly from the bulk InAs bands due to the coupling to the metallic As states. Most of the bands in the junction come from a mixture of all In, As and Al orbitals. However, we have identified an equivalent to the bottom of the bulk InAs conduction band for the case of the heterojunction. And we calculate how the energy difference $\Delta E(k)$ between the SOC spin-split bands (around the Γ point) varies with the rescaling to the SOC.

Figure 6 shows the energy difference $\Delta E(k)$ of the spin-split bands around the Γ point, bands encircled in red in Fig. 5, versus the k-vector along the $\Gamma - Qy$ direction. The spin splitting is more important (for small k values away from Γ) when the SOC rescaling in applied to all In and As atoms, instead of only on the interface In, As atoms. However, it is clear that, in both cases, the spin splitting $\Delta E(k)$ is linear in k (for $k/Qy < 0.1$), which is most probably the signature of the 2D like character of the corresponding states parallel to the InAs/Al interface[43].

It is also interesting to check how the linear dependence of the spin splitting varies with the rescaling of the SOC. We determine the slope of the linear relation $\Delta E(k) \equiv \alpha k$ for small k values (for $k/Qy < 0.05$). The dependence of α(soscl) on the SOC rescaling is shown in panel (c) of Figure 6. We obtain a linear dependence on SOC rescaling when the rescaling is applied to all In and As atoms, and a sublinear dependence when the rescaling is only applied to the interface In,As atoms, indicating different screening effects on the local SOC rescaling.

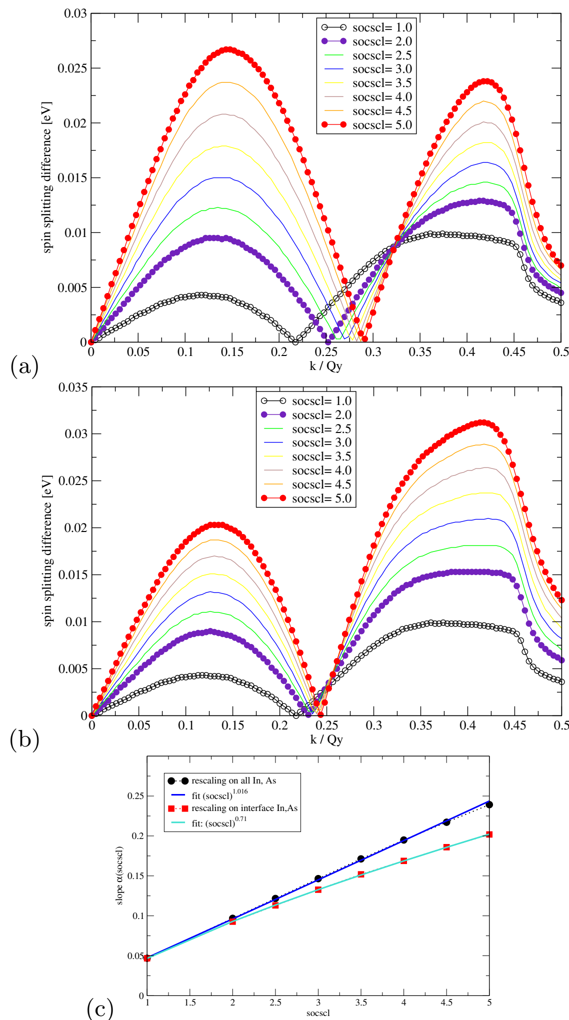

FIG. 6. Energy difference $\Delta E(k)$ of the spin-split bands around the Γ point in the $\Gamma - Qy$ direction. The rescaling (soscl) of the spin-orbit coupling is applied to all In and As atoms in panel (a), to only the In and As interface atoms in panel (b). In both cases, the spin splitting is linear in k for $k/Qy < 0.1$ around each band crossing, i.e. $\Delta E(k) \equiv \alpha k$. Panel (c): dependence of the slope of $\Delta E(k) \equiv \alpha k$ upon the rescaling soscl of the spin-orbit coupling.

IV. CONCLUSION

We have studied the electronic structure of realistic Al/InAs/Al heterojunctions using a combination DFT with hybrid functionals and state-of-the-art QSGW calculations. The InAs/Al heterojunctions we considered are central to superconducting induced properties in InAs and to the design of topological quantum computation platforms. The InAs/Al heterojunctions are described at the atomic level and include atomic relaxations at the InAs/Al interfaces. Our study confirm the need of well controlled quality of the interfaces to obtain the needed properties of InAs/Al heterojunctions. The local band alignment (i.e. top of VB, bottom of CB) obtained from QSGW for semiconductor/metal interfaces can be well reproduced using dielectric-dependent hybrid functional DFT with the novel metallic estimator which automatically switches off the Fock exchange within the bulk of the metal. The prediction of an accumulation layer for InAs/Al is in agreement with experimental evidence. The HSE06+DDH method appears to provide an effective approximation to the full QSGW for this system, and open new paths for exploring larger interface cells or multiple different interface configurations in relation with experimental devices. Furthermore, a detailed analysis of the effects of spin-orbit coupling on the spin-splitting of some electronic states show a linear scaling in k-space. A behaviour most probably related to the two-dimensional nature of the interface states. Our work indicates the possibility of tailoring the properties of the electronic states central to the realisation of topological computers from the quality of the semiconductor/metal interface.

ACKNOWLEDGMENTS

This work was authored by the National Renewable Energy Laboratory, operated by Alliance for Sustainable Energy, LLC, for the U.S. Department of Energy (DOE) under Contract No. DE-AC36-08GO28308, funding from Office of Science, Basic Energy Sciences, Division of Materials. We acknowledge the use of the National Energy Research Scientific Computing Center, under Contract No. DE-AC02-05CH11231 using NERSC award BES-ERCAP0021783 and we also acknowledge that a portion of the research was performed using computational resources sponsored by the Department of Energy's Office of Energy Efficiency and Renewable Energy and located at the National Renewable Energy Laboratory. For early stages of this work, HN and MvS acknowledge financial support from Microsoft Station Q via a sponsor agreement between KCL and Microsoft Research.

HN, DP and MvS acknowledge the Partnership for Advanced Computing in Europe (PRACE) for awarding us access to Juwels Booster and Cluster (Jülich, Germany).

Appendix A: Questaal on GPU

Due to the relatively large simulation cell for QSGW standards, together with (i) relatively dense Brillouin zone sampling and (ii) high angular momentum cutoffs required, the all-electron, the full frequency QSGW calculations are rather difficult to achieve. They were only made practical with the efficient use of new clusters with high-density, high-memory GPU nodes and good interconnect.

Algorithmic improvements avoided most of the filesystem IO. Together with a more flexible memory management, they allowed efficient parallelisation across multiple levels of processes and threads enabling various launch configurations. Nearly all of the remaining IO

was moved to parallel HDF5 maintaining the same file layout independent of the parallelism.

The screened Coulomb potential and the mixed product basis projectors occupy the bulk of the memory available and in the present case could not fit together entirely; fortunately the projectors can be generated and used in piecewise fashion with little overhead.

In the GPU context, each device is handled by a thread allowing simple use of multiple devices per process. The threads distribute batches of matrix operations across dynamically estimated number of streams depending on dimensions and the available memory. In this way host-device transfers and kernel launches are overlapped through asynchronous executions, hiding latency and maximising occupancy and efficiency.

Most of the compute routines make heavy use of the performance libraries cuBLAS, cuSOLVER, cuFFT and cuSPARSE in this mode. Certain larger matrix operations were done collectively with cuSOLVERMg (cu*Mp were not available at the time).

The heaviest step in the computations is the calculation of the full off-diagonal self-energy, it sustained close to 20 PFLOPS on the Juwels-Booster cluster using 288 nodes.

Appendix B: Local DDH functional with metallic correction using localized orbitals

1. DDH overview

The exchange-correlation energy in HSE is constructed by splitting up the Coulomb interaction in a long and short range part using the error functions

$$\frac{1}{r} = \frac{\mathrm{erf}(\omega r)}{r} + \frac{\mathrm{erfc}(\omega r)}{r} \ ,$$

in which ω is a range separation parameter that determines what is defined as long and short range. The exchange correlation energy is then split up as:

$$\begin{aligned} E_{xc}^{\mathrm{HSE}} =& \alpha E_x^{\mathrm{HF,SR}} + (1-\alpha) E_x^{\mathrm{PBE,SR}}(\omega) \\ &+ E_x^{\mathrm{PBE,LR}}(\omega) + E_c^{\mathrm{PBE}} \ . \end{aligned}$$

The amount of *exact* exchange included is determined by α, the exchange fraction. In HSE it is taken to be a constant of 0.25, which is reasonably accurate for medium gap semiconductors but produces some errors for large and small gaps. This is because one can derive that the value of α should be related to the dielectric constant of the material, which is in turn related to the screening. The DDH approach is to create a hybrid functional for which the exchange fraction is determined self-consistently based on the dielectric constant. This is too computationally expensive to calculate, and so an estimator for the dielectric function is used instead (as presented in Refs. 38 and 39):

$$\bar{g} = \frac{1}{V} \int d\mathbf{r} \ \sqrt{\frac{\nabla \rho(\mathbf{r})}{\rho(\mathbf{r})}} \ .$$

The exchange fraction is then related to this estimator by a quartic function:

$$\alpha_{\mathrm{ddh}} = a_0 + a_4 \bar{g}^4 ,$$

which we have fitted to the correct experimental band gap for a large set of semiconductors and insulators.

2. Local DDH using localized orbitals

To study interfaces, it might be that different values of the exchange fraction are needed in different parts of the system. This is why a local estimator is introduced:

$$\bar{g}(\mathbf{r}, \sigma) = \frac{1}{(2\pi\sigma)^{\frac{3}{2}}} \int d\mathbf{r}' \ \sqrt{\frac{\nabla \rho(\mathbf{r}')}{\rho(\mathbf{r}')}} \exp\left(-\frac{|\mathbf{r}-\mathbf{r}'|^2}{2\sigma}\right) \ ,$$

from which we can calculate an exchange fraction field

$$a(\mathbf{r}, \sigma) = a_0 + a_4 \bar{g}(\mathbf{r}, \sigma)^4 .$$

In Ref. 39 this is used in the calculation of the integrals, so that the exchange matrix becomes

$$X_{ij} = \sum_{kl} V_{ik;jl} D_{kl} \ ,$$

where the integrals are defined as:

$$V_{ik;jl} = \int d\mathbf{r} d\mathbf{r}' \phi_i(\mathbf{r}) \phi_k(\mathbf{r}) \alpha(\mathbf{r}, \mathbf{r}'; \sigma) K(|\mathbf{r}-\mathbf{r}'|) \phi_j(\mathbf{r}') \phi_l(\mathbf{r}') \ ,$$

with

$$\alpha(\mathbf{r}, \mathbf{r}'; \sigma) = \sqrt{a(\mathbf{r}, \sigma) a(\mathbf{r}', \sigma)}$$

and K the short range Coulomb kernel.

Instead of recalculating the integrals we use the fact that in QuantumATK a resolution of identity (RI)[44] approach is used to calculate the Coulomb integrals:

$$V_{ik;jl} \approx C_{ik}^{\mu} V_{\mu\nu} C_{jl}^{\nu} \ ,$$

with the introduction of an auxiliary basis $P_\mu(\mathbf{r})$ such that

$$\phi_i(\mathbf{r}) \phi_j(\mathbf{r}) = \sum_\mu C_{ij}^\mu P_\mu(\mathbf{r}) \ .$$

We assume that the auxiliary basis coefficients, C_{ij}^μ are unaffected, and only the integrals between the auxiliary basis functions change:

$$\begin{aligned} V_{\mu\nu} =& \int d\mathbf{r} d\mathbf{r}' \tilde{\phi}_\mu(\mathbf{r}) \alpha(\mathbf{r}, \mathbf{r}'; \sigma) K(|\mathbf{r}-\mathbf{r}'|) \tilde{\phi}_\nu(\mathbf{r}') \\ \approx& \sqrt{\bar{a}_\mu \bar{a}_\nu} \int d\mathbf{r} d\mathbf{r}' \tilde{\phi}_\mu(\mathbf{r}) K(|\mathbf{r}-\mathbf{r}'|) \tilde{\phi}_\nu(\mathbf{r}') \ , \end{aligned}$$

in which we have taken a Gaussian average of the a coefficients around the center they are located on:

$$\bar{a}_\mu(\sigma,\tau) = \int d\mathbf{r} a(\mathbf{r},\sigma) \exp\left(-\frac{|\mathbf{r}-\mathbf{r}_\mu|^2}{2\tau}\right) . \quad \text{(B1)}$$

The approximation being made here is that the local estimator is approximately constant or at least slowly varying over the region where a single auxiliary basis function has support, which is on a center.

3. Metallic correction to local DDH

For metals there is perfect screening, and we would expect the exchange fraction to go down to zero. Unfortunately the DDH method doesn't reproduce this behaviour. This is why we introduce a second *metallic* estimator. At every step of the self-consistent loop we calculate the Fermi level density matrix

$$\mathcal{F}_{ij} = \sum_{\mathbf{k}} \sum_n \exp\left[-\frac{(\epsilon_F - \epsilon_{\mathbf{k},n})^2}{2\sigma_F}\right] \langle\phi_i|\psi_{\mathbf{k}n}\rangle\langle\psi_{\mathbf{k}n}|\phi_j\rangle ,$$

where σ_F is the Fermi level broadening, chosen to be 0.001 eV. This is used to calculate the Fermi level density

$$f(\mathbf{r}) = \sum_{ij} \mathcal{F}_{ij}\phi_i(\mathbf{r})\phi_j(\mathbf{r}) .$$

We then define the following metallic estimator function:

$$\begin{aligned} M(\mathbf{r}) &= 1 \quad \text{if} \quad f(\mathbf{r}) < c_\mu \\ M(\mathbf{r}) &= 0 \quad \text{if} \quad f(\mathbf{r}) \geq c_\mu \end{aligned}$$

where c_μ is a cutoff parameter we have chosen to be 0.0003. This function is convoluted with a Gaussian to get a smooth metallic estimator function:

$$m(\mathbf{r}) = \int d\mathbf{r}' M(\mathbf{r}') \exp\left(-\frac{|\mathbf{r}-\mathbf{r}'|^2}{2\sigma_\mu}\right) ,$$

where the width of the Gaussian is chosen to be 1 Å. We then multiply the metallic estimator with the function $a(\mathbf{r},\sigma)$:

$$a_m(\mathbf{r},\sigma) = m(\mathbf{r})a(\mathbf{r},\sigma) ,$$

before the averaging around a center is performed in Eq. (B1).

[1] J. D. Sau, R. M. Lutchyn, S. Tewari, and S. Das Sarma, Phys. Rev. Lett. **104**, 040502 (2010).
[2] J. Alicea, Phys. Rev. B **81**, 125318 (2010).
[3] R. M. Lutchyn, J. D. Sau, and S. Das Sarma, Phys. Rev. Lett. **105**, 077001 (2010).
[4] Y. Oreg, G. Refael, and F. von Oppen, Phys. Rev. Lett. **105**, 177002 (2010).
[5] J. Alicea, Reports on Progress in Physics **75**, 076501 (2012).
[6] M. Leijnse and K. Flensberg, Semiconductor Science and Technology **27**, 124003 (2012).
[7] C. Beenakker, Annual Review of Condensed Matter Physics **4**, 113 (2013).
[8] M. F. S. Das Sarma and C. Nayak, NPJ Quant. Inf. **1**, 15001 (2015).
[9] R. Aguado, Riv. Nuovo Cimento **40**, 523 (2017).
[10] R. M. Lutchyn, E. P. A. M. Bakkers, L. P. Kouwenhoven, P. Krogstrup, C. M. Marcus, and Y. Oreg, Nature Reviews Materials **3**, 52 (2018).
[11] C. Nayak, S. H. Simon, A. Stern, M. Freedman, and S. Das Sarma, Rev. Mod. Phys. **80**, 1083 (2008).
[12] M. Aghaee and et. al., (2024), arXiv:2401.09549 [cond-mat.mes-hall].
[13] P. Krogstrup, N. Ziino, W. Chang, and et al., Nature Mater. **14**, 400 (2015).
[14] H. J. Suominen, M. Kjaergaard, A. R. Hamilton, J. Shabani, C. J. Palmstrøm, C. M. Marcus, and F. Nichele, Phys. Rev. Lett. **119**, 176805 (2017).
[15] F. Nichele, A. C. C. Drachmann, A. M. Whiticar, E. C. T. O'Farrell, H. J. Suominen, A. Fornieri, T. Wang, G. C. Gardner, C. Thomas, A. T. Hatke, P. Krogstrup, M. J. Manfra, K. Flensberg, and C. M. Marcus, Phys. Rev. Lett. **119**, 136803 (2017).
[16] S. Vaitiekénas, A. M. Whiticar, M.-T. Deng, F. Krizek, J. E. Sestoft, C. J. Palmstrøm, S. Marti-Sanchez, J. Arbiol, P. Krogstrup, L. Casparis, and C. M. Marcus, Phys. Rev. Lett. **121**, 147701 (2018).
[17] S. Matsuo, M. Tateno, Y. Sato, K. Ueda, Y. Takeshige, H. Kamata, J. S. Lee, B. Shojaei, C. J. Palmstrøm, and S. Tarucha, Phys. Rev. B **102**, 045301 (2020).
[18] G. C. Ménard, G. L. R. Anselmetti, E. A. Martinez, D. Puglia, F. K. Malinowski, J. S. Lee, S. Choi, M. Pendharkar, C. J. Palmstrøm, K. Flensberg, C. M. Marcus, L. Casparis, and A. P. Higginbotham, Phys. Rev. Lett. **124**, 036802 (2020).
[19] S. Vaitiekenas, G. W. Winkler, B. van Heck, T. Karzig, M.-T. Deng, K. Flensberg, L. I. Glazman, C. Nayak, P. Krogstrup, R. M. Lutchyn, and C. M. Marcus, Science **367** (2020).
[20] M. W. A. de Moor, J. D. S. Bommer, D. Xu, G. W. Winkler, A. E. Antipov, A. Bargerbos, G. Wang, N. van Loo, R. L. M. O. het Veld, S. Gazibegovic, D. Car, J. A. Logan, M. Pendharkar, J. S. Lee, E. P. A. M. Bakkers, C. J. Palmstrøm, R. M. Lutchyn, L. P. Kouwenhoven, and H. Zhang, New Journal of Physics **20**, 103049 (2018).
[21] J. Shen, S. Heedt, F. Borsoi, and et al., Nat. Commun. **9**, 4801 (2018).

[22] G. L. R. Anselmetti, E. A. Martinez, G. C. Ménard, D. Puglia, F. K. Malinowski, J. S. Lee, S. Choi, M. Pendharkar, C. J. Palmstrøm, C. M. Marcus, L. Casparis, and A. P. Higginbotham, Phys. Rev. B **100**, 205412 (2019).
[23] X. D. S. V. Op het Veld, R.L.M. and et al., Commun. Phys. **3**, 59 (2020).
[24] T. Kanne, M. Marnauza, D. Olsteins, and et al., Nat. Nanotechnol. **16**, 776 (2021).
[25] M. Pendharkar, B. Zhang, H. Wu, A. Zarassi, P. Zhang, C. P. Dempsey, J. S. Lee, S. D. Harrington, G. Badawy, S. Gazibegovic, R. L. M. O. het Veld, M. Rossi, J. Jung, A.-H. Chen, M. A. Verheijen, M. Hocevar, E. P. A. M. Bakkers, C. J. Palmstrøm, and S. M. Frolov, Science **372**, 508 (2021).
[26] J. L. N. Tomaszewska, L. Walczak and J. J. Kolodziej, Surface Science **632**, 103 (2015).
[27] S. Schuwalow, N. B. M. Schröter, J. Gukelberger, C. Thomas, V. Strocov, J. Gamble, A. Chikina, M. Caputo, J. Krieger, G. C. Gardner, M. Troyer, G. Aeppli, M. J. Manfra, and P. Krogstrup, Advanced Science **8**, 2003087 (2021).
[28] S. Yang, N. B. M. Schrter, V. N. Strocov, S. Schuwalow, M. Rajpalk, K. Ohtani, P. Krogstrup, G. W. Winkler, J. Gukelberger, D. Gresch, G. Aeppli, R. M. Lutchyn, and N. Marom, Advanced Quantum Technologies **5**, 2100033 (2022).
[29] R. Batabyal, S. Zelzer, A. P. Romagosa, D. Dardzinski, F. Corsetti, N. Marom, and P. Krogstrup, Phys. Rev. Mater. **7**, 066201 (2023).
[30] A. V. Krukau, O. A. Vydrov, A. F. Izmaylov, and G. E. Scuseria, The Journal of Chemical Physics **125**, 224106 (2006).
[31] "Questaal code website," `https://www.questaal.org`.
[32] S. Smidstrup, T. Markussen, P. Vancraeyveld, J. Wellendorff, J. Schneider, T. Gunst, B. Verstichel, D. Stradi, P. A. Khomyakov, U. G. Vej-Hansen, M.-E. Lee, S. T. Chill, F. Rasmussen, G. Penazzi, F. Corsetti, A. Ojanperä, K. Jensen, M. L. N. Palsgaard, U. Martinez, A. Blom, M. Brandbyge, and K. Stokbro, J. Phys.: Condens. Matter **32**, 015901 (2019).
[33] D. Pashov, S. Acharya, W. R. Lambrecht, J. Jackson, K. D. Belashchenko, A. Chantis, F. Jamet, and M. van Schilfgaarde, Comput. Phys. Commun **249**, 107065 (2020).
[34] S. V. Faleev, M. van Schilfgaarde, and T. Kotani, Phys. Rev. Lett. **93**, 126406 (2004).
[35] T. Kotani, M. van Schilfgaarde, and S. V. Faleev, Phys. Rev. B **76**, 165106 (2007).
[36] B. Cunningham, M. Grüning, D. Pashov, and M. van Schilfgaarde, Phys. Rev. B **108**, 165104 (2023).
[37] A. L. Kutepov, Phys. Rev. B **95**, 195120 (2017).
[38] M. A. L. Marques, J. Vidal, M. J. T. Oliveira, L. Reining, and S. Botti, Phys. Rev. B **83**, 035119 (2011).
[39] P. Borlido, M. A. L. Marques, and S. Botti, J. Chem. Theory Comput. **14**, 939 (2018), pMID: 29227686.
[40] A. V. Krukau, O. A. Vydrov, A. F. Izmaylov, and G. E. Scuseria, J. Chem. Phys. **125**, 224106 (2006).
[41] M. van Setten, M. Giantomassi, E. Bousquet, M. Verstraete, D. Hamann, X. Gonze, and G.-M. Rignanese, Comput. Phys. Commun. **226**, 39 (2018).
[42] M. Guidon, J. Hutter, and J. VandeVondele, J. Chem. Theory Comput. **6**, 2348 (2010), pMID: 26613491.
[43] J.-W. Luo, A. N. Chantis, M. van Schilfgaarde, G. Bester, and A. Zunger, Phys. Rev. Lett. **104**, 066405 (2010).
[44] X. Ren, P. Rinke, V. Blum, J. Wieferink, A. Tkatchenko, A. Sanfilippo, K. Reuter, and M. Scheffler, New J. Phys. **14**, 053020 (2012).

Appendix C: Supplementary Material

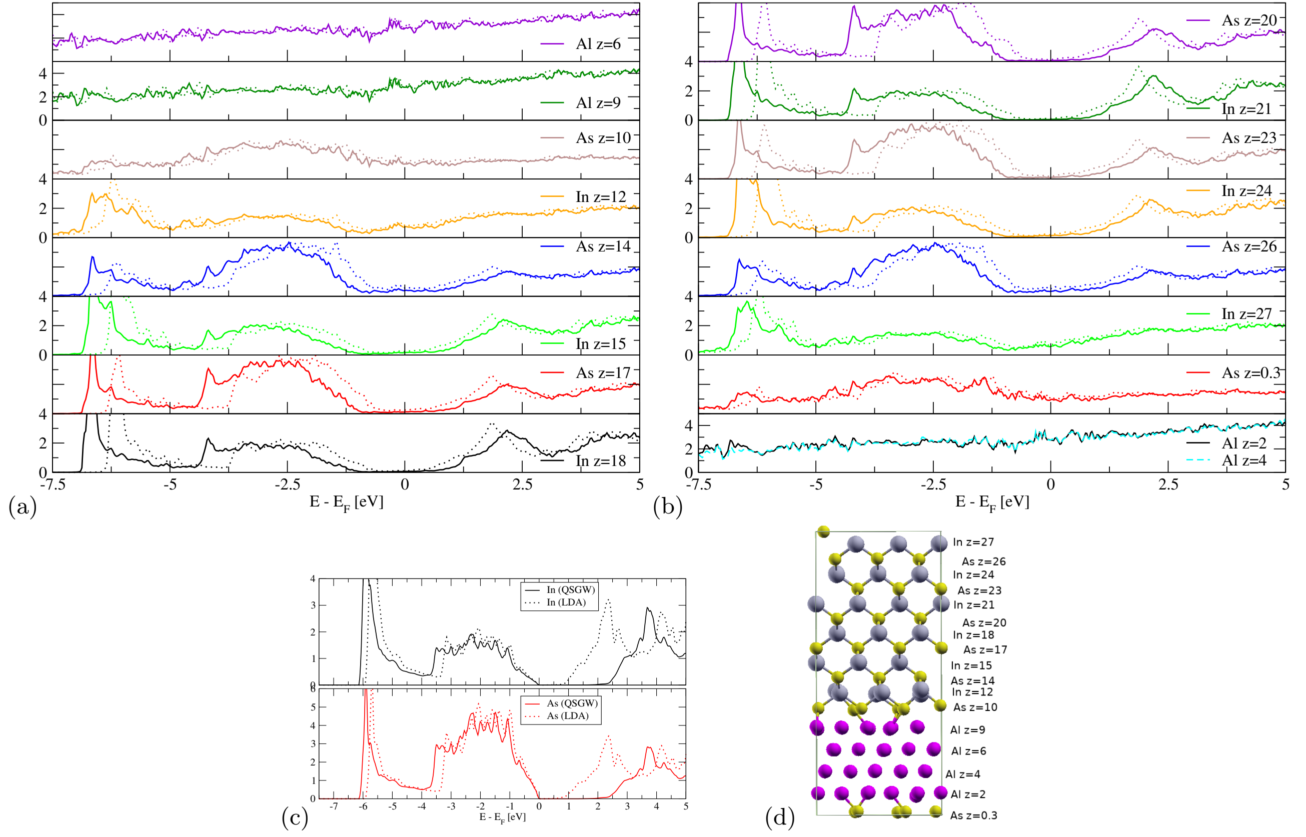

FIG. 7. Local density of states LDOS per atomic layers in the InAs/Al heterojunction, panels (a) and (b), obtained from QS*GW* (solid lines) and LDA (dotted lines) calculations. Panel (c) shows the corresponding bulk LDOS, panel (d) shows the labelling of the atomic layers in the z-direction. The LDOS of the central In and As atomic layers, labelled $z = 18, 20, 21$, are similar to the bulk LDOS. The LDOS of the In and As atomic layers acquires a stronger admixture with the Al states, the closer the layers are to the InAs/Al interfaces. Note that in the bulk LDOS, the Fermi energy E_{F} is located at the top of the valence band as a convention for any semiconductors at zero temperature. For the heterojunction, the position of E_{F} is governed by the metallic states of the Al slab.

1. Local density of states

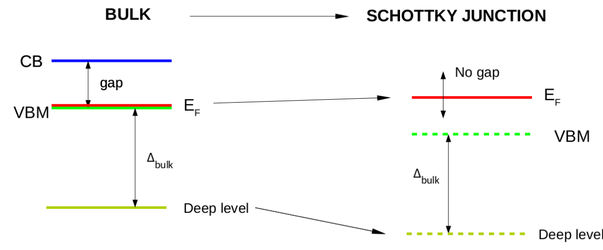

FIG. 8. Schematic representation of the modifications of the In and As deep electronic levels upon changing atoms from a bulk configuration to a InAs/Al heterojunction configuration.

2. Transition bulk to heterojunction

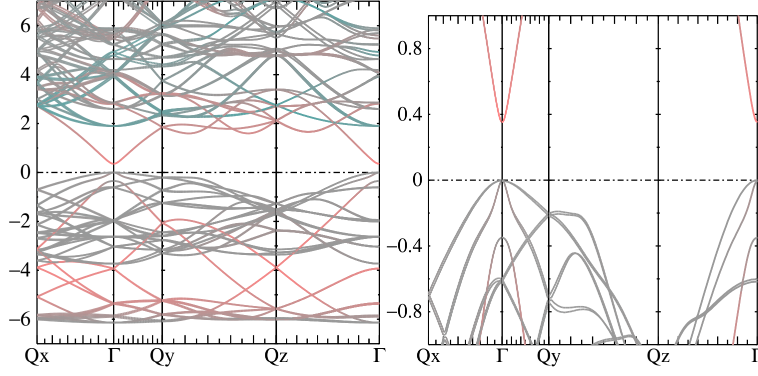

FIG. 9. QSGW Bulk band structure of InAs. Energies are given in eV. For allowing direct comparisons between bulk and heterojunction systems, the bulk bands have been calculated for a cell having the same lattice vectors $u_{1,2}$ in the (001) plane as for the InAs/Al heterojunction. Qx, y, z represents the (x,y,z)-direction in the reciprocal space. The color scheme represent the weight of the As s-orbital in the bands: red: large weight of As s-orbital, grey/black: no As s-orbital weight. One can see that the bottom of the conduction band is mostly consisting of As s-states. This color scheme will be useful to identify the "bulk InAs conduction band" in the band structure of the InAs/Al heterojunction.

3. Band structure

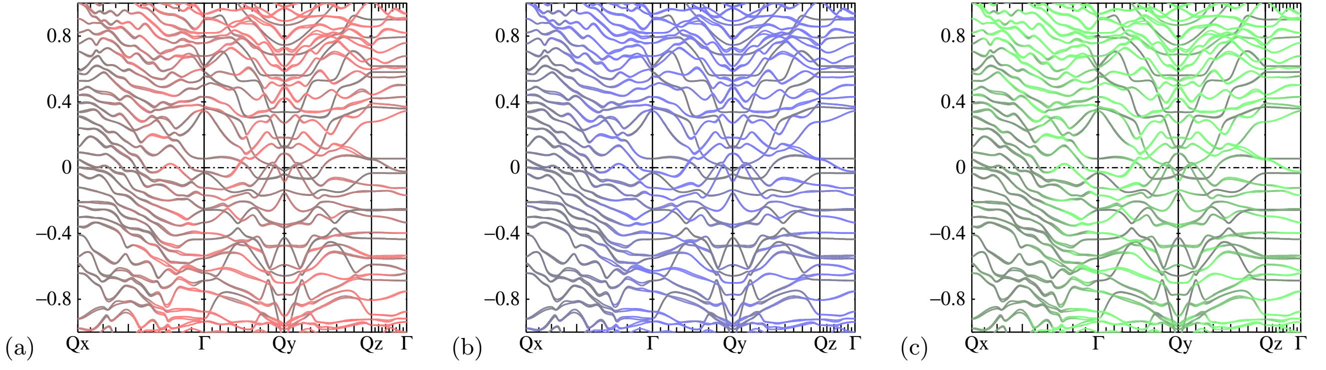

FIG. 10. QSGW band structure of the InAs/Al heterojunction made of 138 atoms. Energies are given in eV. The band structure look much more complex than for bulk InAs due to the large size of the system, the presence of the Al metallic states and the relaxation of the InAs/Al interfaces. There is clearly no band gap anymore in the heterojunction. The bands in panels (a), (b), (c) are colored in red, blue, green respectively according to the projection weight of the states onto the bulk-like atomic layers of As $z = 20$, In $z = 18$, In $z = 21$. See panel (d) in Fig. 7 for the z-direction labelling. There is a strong mixing of all As and In orbitals in the bands, as well as mixing with Al orbitals. Note the two flat bands around $E_{\rm F}$ along the $\Gamma - Qz$ direction implying the existence of localized "interface" states. This states are however delocalised in the (xy) planes of the InAs/Al interfaces. A careful analysis of the composition of these states (not shown here) reveal that they consist mostly of orbitals of the As $z = 10$ and Al $z = 9$ (and of the As $z = 0.3$ and Al $z = 2$) atomic layers.

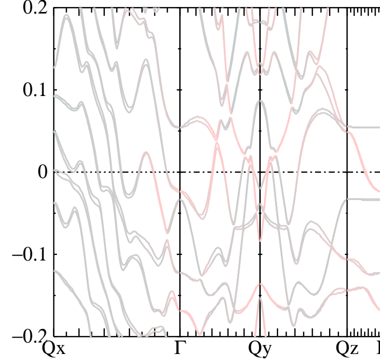

FIG. 11. QSGW band structure of the InAs/Al heterojunction made of 138 atoms. Energies are given in eV. Zoom in energy of the bands shown in Fig. (10). The bands are colored in red according to the projection weight of the states onto the s-orbitals of the bulk-like atomic layers of As $z = 20$. In Fig. (9), we have seen that the bottom of the bulk InAs conduction band, around the Γ point, is mostly of As s-character. For the InAs/Al heterojunction, we can see that some bands around the Γ point, still keep a non-negligible weight of the bulk-like As s-orbitals; more specially the bands ~ 50 meV below $E_{\rm F}$. This energy position below $E_{\rm F}$ corresponds well with our estimate of the energy shift of the bulk-like conduction band minimum shown in Fig. (2). We therefore consider that these bands are the equivalent of the bottom of the bulk-like conduction band of InAs which strongly couples to the Al states in the InAs/Al heterojunction.

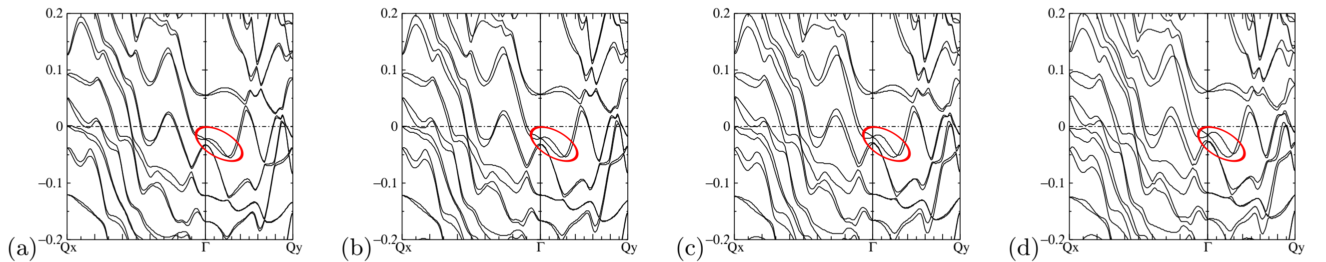

FIG. 12. QSGW band structure of the InAs/Al heterojunction made of 138 atoms, for different rescaling of the SOC. Panel (a), (b), (c) and (d) corresponds to rescaling the original SOC by $\times 2, \times 3, \times 4$ and $\times 5$ respectively. Focussing on the bands around the Γ point and at $E \sim E_{\rm F} - 0.05$, one can see the spin-split bands (due to SOC) along the $\Gamma - Qy$ direction. The splitting between the two bands increases with increasing rescaling of the SOC, as expected.